# Congested shallow water model: trapped air pockets modeling

Martin Parisot

# CONGESTED SHALLOW WATER MODEL: TRAPPED AIR POCKETS MODELING*

MARTIN PARISOT†

**Abstract.** In this work, the modeling and numerical resolution in the multidimensional framework of the interaction between the congested shallow water model and a polytropic air pocket dynamics are addressed. A weak coupling strategy is adopted and the air pocket connectivity is obtained by comparing there horizontal supports. Several numerical simulations illustrate the relevance of the model and the robustness of the numerical strategy. In particular, the method seems well suited to the numerical study of the hydraulics of underground rivers and coastal caves such as the Cosquer cave, and to the simulation of the marine energy converter such as the oscillating water column.

**Key words.** Congested shallow water model, Polytropic gaz dynamics, Liquid-gas two-phase problem, Nonlinear integro-differential equations, Pipe flows, Immersed cave hydrodynamics, Renewable marine energy

**MSC codes.** 35L60, 76T10, 76B07, 76M12, 86-08

**1. Introduction.** This work focuses on flows, both free surface and roof constrained, showing air pockets whose evolution can significantly affect the flow. This type of flow can be found in the natural environment in underground rivers, in submerged coastal caves [14] or under the ice pack, in pipe flow, especially sewage in case of flooding or pumping [29], and for several marine energy converter devices such as the oscillating water column [18, §6]. Paradoxically, the air pocket modeling is necessary to avoid the formation of (vacuum) pockets, and in particular the simulation of pumping in deep aquifers [22].

The modeling of air pockets above a free-surface flow is a two-phase liquid-gas problem [13, 28]. There is a large literature on this issue both from the point of view of modeling and numerical resolution [35], especially in the context of flow in a pipe. According to the applications, two types of models are described: the incompressible two-phase model [3, 11, 12] for two-fluid problems, or the compressible two-phase model [15, 25] for problems with gas. The complexity of these models makes numerical simulation impossible at the scale of interest here (several $km^3$). In our geophysical flow context, reduced models of water wave equations such as shallow water models are usually used [27]. To take into account the roof constraint, a particular modeling and numerical scheme have been proposed in the literature [5, 8, 10, 20, 26]. The current work is devoted to coupling with the air pressure in the air pocket that can form between the free surface and the roof. This issue with vertical integrated models has been considered in [1] for incompressible flows. In our context, the air phase cannot be considered as incompressible because its domain, complement of the water domain in the opening see Fig. 1, is an unknown of the problem. In [9], the authors propose an integrated incompressible/compressible model for the liquid-gas problem. Nevertheless, the model is well posed (hyperbolic) only for a small or large relative speed between the two phases. In [19], a two-fluid two-pressure vertical integrated model is proposed. This work concludes on the remark that the speed of sound is large even in the air phase. This means that the relaxation time of the pressure in the air phase is small enough to consider quasi-steady air dynamics. Our approach is based on a polytropic modeling of the air pocket dynamics [33]. Air pocket merging and splitting are taken into account to allow for several different application contexts and increase the robustness of the method. The proposed model is nonlinear, hyperbolic with

*Submitted to the editors August 9, 2022.

**Funding:** research project ANR-19-CE46-0010-01 GeoFun.

†INRIA, Univ. Bordeaux, CNRS, Bordeaux INP, IMB, UMR 5251, 200 Avenue de la Vieille Tour, 33405 Talence cedex, France (martin.aparisot@inria.fr).

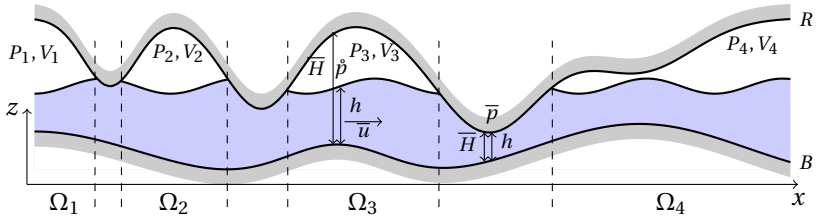


FIG. 1. *Illustration of the unknowns of the congested shallow water model with air pockets modeling* (2.1), (2.2), (2.3), (2.4), (2.5), (2.6), (2.7) *and* (2.8).

congested areas (leading locally to elliptical behavior), and integro-differential (due to the air pressure calculated from the pocket volume). To avoid the resolution of a large stencil matrix, we propose a weak coupling between the water and air dynamics. Thanks to these choices, the numerical resolution of the model is quite fast compared to the cited literature, which allowed us to simulate scenarios with a sensitivity analysis of some parameters as illustrated in the §5.5.

**2. Mathematical modeling.** This section is devoted to the mathematical description of the free-surface flow constrained by a roof and coupled with air pocket dynamics using a vertical integrated model. Let us first describe the unknowns used and illustrated in Fig. 1. On a horizontal domain $x \in \Omega \subset \mathbb{R}^D$ with $D \in \{1,2\}$, we consider two given surfaces $B(t,x) \leq R(t,x)$ playing respectively the role of the bathymetry and the roof. Between the two surfaces, a shallow water type model is considered following [20]. More precisely, the unknowns are the mean vertical velocity $\overline{u}(t,x)$ and the water depth $h(t,x)$, see §2.1. Where the flow reaches the roof, i.e. $h = \overline{H}$ with the opening $\overline{H} = R - B$, the roof reaction acts as a surface pressure $\overline{p}(t,x)$ so that the flow remains restricted by the roof. In this previous work, the pressure in the air is considered as a given parameter. However, it does not correspond to several physical experiments like Torricelli's experiment, see §5.2. To overcome this drawback, we assume that the air can be considered as a polytropic gas, then the air pressure $\mathring{p}(t,x)$ is an unknown satisfying the Laplace law.

**2.1. Fluid modeling.** We briefly recall the congested shallow water model as proposed in [20]. The congested shallow water model reads

$$\begin{aligned} \partial_t h + \nabla \cdot \left(h\overline{u}\right) &= 0 \\ \partial_t \left(h\overline{u}\right) + \nabla \cdot \left(h\overline{u} \otimes \overline{u}\right) &= -h\nabla\phi\left(h, \overline{p}, \mathring{p}, B\right) \end{aligned} \tag{2.1}$$

with the potential of conservative forces

$$\phi\left(h, \overline{p}, \mathring{p}, B\right) = g\left(B + h\right) + \frac{\overline{p} + \mathring{p}}{\rho} \tag{2.2}$$

and the density of the water $\rho > 0$. The pressure acting on the flow at the surface of the flow is decomposed into the roof reaction $\overline{p}(t,x)$ and the pressure in the air $\mathring{p}(t,x)$. In [20], the air pressure $\mathring{p}$ in not modeled but assumed to be a given parameter, and in practice it is set to zero. The roof reaction $\overline{p}$ is such that the water depth remains below the roof. As mentioned in [20], the model is not well-posed without looking for the roof reaction among the positive functions. More precisely, it is sought so that the following constraint is satisfied

$$\min\left(\overline{H} - h, \overline{p}\right) = 0. \tag{2.3}$$

The solution where the water level sticks to the roof exists when there is no connection with the air above the water, see §5.2. In [10], the authors propose a numerical strategy based on the neighbors to determine if the air can reach the roof. However, this solution does not fixe all situations, for exemple is does not recover all the possible steady states, see §5.1.

**2.2. Air pockets modeling.** As Baliani explained in 1630, water is not attracted by the roof but pushed by the air outside the cavity. We assume here that the relaxation time of the pressure in the air is small enough so that the pressure is uniform by pockets, ie.

$$\mathring{p}(t,x) = \sum_{i=1}^{N_p\left(\overline{h}\right)} P_i(t)\,\mathbb{1}_{\Omega_i\left(\overline{h}\right)}(x) \qquad \text{with} \qquad \overline{h} = \overline{H} - h \tag{2.4}$$

where $N_p\left(\overline{h}\right) \in \mathbb{N}$ is the number of pockets, defined by the number of connexe sets of support of $\overline{h}$, and $\Omega_i\left(\overline{h}\right) \subset \Omega$ is the support of the $i^{\text{th}}$ pocket, defined for $1 \le i \le N_p\left(\overline{h}\right)$ by the $i^{th}$ connexe set of support of $\overline{h}$ (the order of numbering from 1 to $N_p$ has no impact). It remains to define the pressure values $P_i(t)$. Note that the pressure $\mathring{p}(t,x)$ has no physical meaning outside the pockets $x \notin \Omega_i$ but must be defined for the relevance of the model (2.1). Similar to the roof reaction $\overline{p}$ that disappears where water does not reach the roof, we consider that the air pressure disappears outside the pockets.

Also we assume that the pockets dynamics are governed by three processes, i.e. splitting, deforming and merging, that can be describe mathematically by polytropic laws, see [17, 33]. More precisely, introducing the the volume of the $i^{th}$ pocket as

$$\text{with} \qquad V_i\left(\overline{h}\right) = \int_{\Omega_i\left(\overline{h}\right)} \overline{h}\,\mathrm{d}x, \tag{2.5}$$

the splitting of a pocket at time $t^*$ can be model using a parameter $s \ge 0$ by

$$\begin{aligned} \forall j \in \mathbb{L}_i \qquad & P_j\left(t^*+\varepsilon\right)\left(V_j\left(t^*+\varepsilon\right)\right)^s - P_i\left(t^*-\varepsilon\right)\left(V_i\left(t^*-\varepsilon\right)\right)^s \underset{\varepsilon\to 0}{\longrightarrow} 0 \\ & \text{and} \qquad \sum_{j\in\mathbb{L}_i} V_j\left(\overline{h}\left(t^*+\varepsilon\right)\right) - V_i\left(\overline{h}\left(t^*-\varepsilon\right)\right) \underset{\varepsilon\to 0}{\longrightarrow} 0, \end{aligned} \tag{2.6}$$

the merging of pockets at time $t^*$ can be model using a parameter $m \ge 0$ by

$$\begin{aligned} & \left(P_j\left(t^*+\varepsilon\right)\right)^{1/m} V_j\left(\overline{h}\left(t^*+\varepsilon\right)\right) - \sum_{i\in\mathbb{L}_j} \left(P_i\left(t^*-\varepsilon\right)\right)^{1/m} V_i\left(\overline{h}\left(t^*-\varepsilon\right)\right) \underset{\varepsilon\to 0}{\longrightarrow} 0 \\ & \text{and} \qquad V_j\left(\overline{h}\left(t^*+\varepsilon\right)\right) - \sum_{i\in\mathbb{L}_j} V_i\left(\overline{h}\left(t^*-\varepsilon\right)\right) \underset{\varepsilon\to 0}{\longrightarrow} 0, \end{aligned} \tag{2.7}$$

and meanwhile, the deformation of the pockets can be model using a parameter $d \ge 0$ by

$$\partial_t\left(P_i V_i^d\right) = 0. \tag{2.8}$$

The merger is written so that if pockets with the same pressure merge, regardless of their respective volumes, the resulting pressure should be the pressure in the original pockets. Specific values of the polytropic parameters correspond to a particular physics. Although the present work is designed for general polytropic processes, it is generally accepted that the splitting process is isobaric ($s = 0$), the merging process is adiabatic ($m = \gamma$), while the deformation process, if slow enough, is isothermal ($d = 1$).

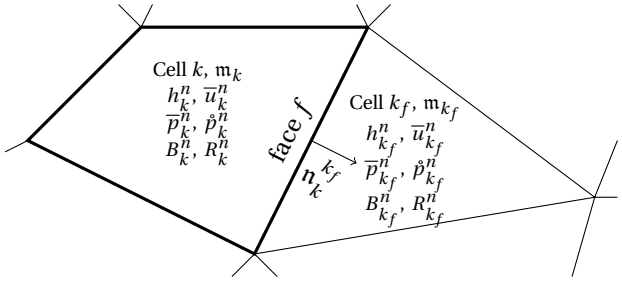


FIG. 2. *Illustration of the unknowns and numerical parameters.*

**2.3. Initial conditions.** In addition to the initial condition of the shallow water model, i.e. $h(0,x) = h^0(x)$ and $\overline{u}(0,x) = \overline{u}^0(x)$, the congested model with air pocket modeling (2.1), (2.2), (2.3), (2.4), (2.5), (2.6), (2.7) and (2.8) requires initialization of the pressure in each pocket. The initial pockets are themselves defined from the initial water surface. From the initial water depth, the bottom and the roof, we get the initial number of pockets $N_p\left(\overline{h}^0\right)$, the initial support of the pocket $\Omega_i\left(\overline{h}^0\right)$ and the initial volume of each pockets $V_i\left(\overline{h}^0\right)$ with $\overline{h}^0(x) = \overline{H}(0,x) - h^0(x)$. For $1 \le i \le N_p\left(\overline{h}^0\right)$, let $P_i^0 \in \mathbb{R}_+$ be the initial pressure in each pocket, i.e. $P_i(0) = P_i^0$.

**2.4. Boundary conditions.** In the current work, we assume that the boundary of the computational domain is not congested. It follows that the model coincides locally with the shallow water model and its boundary conditions can be used for the fluid unknowns. Suppose that the boundary is a wall, the whole pocket is inside the computational domain, its volume can be computed and its evolution satisfies the dynamics presented in §2.2. Otherwise, if the pocket reaches an open bound (fixed discharge, fixed water depth...), the pocket extends outside the computational domain and there is missing information. In this case, we impose the air pressure at the boundary, possibly as a function of time. Note that the latter choice can also be considered for a pocket that is not at the boundary, to model pumping or other devices.

**3. Numerical scheme.** The system (2.1), (2.2), (2.3), (2.4), (2.5), (2.6), (2.7) and (2.8) is not trivial for several reasons. Its mathematical structure is not usual because of the constraint (2.3). Specifically, when the flow is not congested, i.e. $h < \overline{H}$, the system is hyperbolic as a compressible flow, while when the flow is congested, i.e. $h = \overline{H}$, the system is elliptical as an incompressible flow. This difficulty imposes the use of a particularly robust scheme, namely low-Mach and implicit, see [20]. In addition, the models is nonlinear because of (2.1), (2.8) and (2.7). Moreover, it is integro-differential because of the volume computation (2.5). To keep the resolution efficient, we propose a numerical strategy based on a weak coupling. More precisely, the water depth $h$ and the roof reaction $\overline{p}$ are first computed using the velocity $\overline{u}$ and the air pressure $\mathring{p}$ at the previous time step, using an implicit nonlinear scheme with a small stencil. Then the velocity $\overline{u}$ and the air pressure $\mathring{p}$ are computed using respectively an explicit advection scheme and a nonlinear algebraic problem.

We consider a tessellation $\mathbb{T}$ of the computational domain $\Omega$ composed of polygonal control volumes, see Fig. 2. The set of faces of the control volume $k$ is denoted $\mathbb{F}_k$, its area is denoted $\mathfrak{m}_k$ and its neighbor by the face $f \in \mathbb{F}_k$ is denoted $k_f$. For each face of the tessellation, we note $\mathfrak{m}_f$ its length (with the convention $\mathfrak{m}_f = 1$ if $D = 1$) and $\mathfrak{n}_k^{k_f}$ the unit

normal to the face $f$ outward from the control volume $k$. For further use, we also define the compactness of the control volume by $\delta_k = \frac{\mathfrak{m}_k}{\sum_{f\in\mathbb{F}_k}\mathfrak{m}_f}$. The discrete data and the unknowns are $B_k^n, \overline{H}_k^n$ and $\psi_k^n$ as an approximation of the cell-averaged values of bathymetry $B$, the opening $\overline{H}$ and $\psi \in \{h, \overline{u}, \overline{p}, \mathring{p}\}$ at the time $t^n$.

**3.1. Numerical scheme of the fluid dynamics.** Due to the congestion constraint (2.3), the numerical strategy for fluid dynamics must have two properties, namely low-Mach and implicit [20]. Several schemes can be found in the literature see for example [4, 7, 16, 23, 24, 31, 34, 36, 37]. For practical reasons, we use the CPR scheme [31]. We give here a brief description of the computation, see [20] for more details.

A peculiarity of the CPR scheme is that the water depth $h_k^n$ and the roof reaction $\overline{p}_k^n$ are determined secondarily from the potential $\phi_k^n$ which is the real unknown of the implicit part of the scheme. Namely we define from (2.2) the water depth

$$\mathscr{H}_k^n(\phi) = \min\left(\widetilde{h}_k^n(\phi), \frac{\overline{H}_k^n + \lambda_k^2 \widetilde{h}_k^n(\phi)}{1+\lambda_k^2}\right) \qquad \text{with} \quad \widetilde{h}_k^n(\phi) = \frac{\rho\phi - \mathring{p}_k^n}{g\rho} - B_k^n \tag{3.1}$$

with the penetration parameter $\lambda_k \geq 0$ (fixed as $\lambda_k = \sqrt{\frac{L_z}{L_x}\delta_k}$ with $L_x$ and $L_z$ are respectively the horizontal and the vertical characteristic lengths) and the roof reaction

$$\mathscr{P}_k^n(\phi) = \rho\left(\phi - g\left(\mathscr{H}_k^n(\phi) + B_k^n\right)\right) - \mathring{p}_k^n. \tag{3.2}$$

The mass conservation of (2.1) is discretized using an implicit nonlinear finite volume method, i.e. the water depth $\phi_\star^{n+1}$ is defined such that $S_k^n(\phi_\star^{n+1}) = 0$ with

$$S_k^n(\phi_\star) := \mathscr{H}_k^n(\phi_k) - \left(h_k^n - \frac{\delta_t^{n+1}}{\mathfrak{m}_k}\sum_{f\in\mathbb{F}_k}\mathscr{F}_f^n(\phi_\star)\cdot\mathfrak{n}_k^{k_f}\mathfrak{m}_f\right) \tag{3.3}$$

and the numerical mass flux reads

$$\mathscr{F}_f^n(\phi_\star) := \left(\mathscr{H}^n(\phi)\,\overline{u}^n\right)_f - \kappa\delta_t^{n+1}\left(\frac{\mathscr{H}^n(\phi)}{\delta}\right)_f [\phi^{n+1}]_k^{k_f}\,\mathfrak{n}_k^{k_f}$$

where $\kappa \geq 1$ is a regularization parameter and the following notations at the face are used $(\psi)_f := \frac{\psi_k+\psi_{k_f}}{2}$ and $[\psi]_k^{k_f} := \frac{\psi_{k_f}-\psi_k}{2}$. The mass scheme (3.3) is solved using an Newton fixed point, see §4 for details.

Once the potential $\phi_k^{n+1}$ is known, the water depth and the roof reaction are computed using (3.1) and (3.2) setting $h_k^{n+1} := \mathscr{H}_k^n(\phi_k^{n+1})$ and $\overline{p}_k^{n+1} := \mathscr{P}_k^n(\phi_k^{n+1})$. Then the velocity is computed explicitly using an upwind scheme for the advection part and a centered source term of the pressure, i.e.

$$\begin{aligned} h_k^{n+1}\overline{u}_k^{n+1} = h_k^n\overline{u}_k^n - \frac{\delta_t^{n+1}}{\mathfrak{m}_k}h_k^{n+1}\sum_{f\in\mathbb{F}_k}(\phi^{n+1})_f\cdot\mathfrak{n}_k^{k_f}\mathfrak{m}_f. \\ -\frac{\delta_t^{n+1}}{\mathfrak{m}_k}\sum_{f\in\mathbb{F}_k}\left(\overline{u}_k^n\left(\mathscr{F}_f^n(\phi_\star^{n+1})\cdot\mathfrak{n}_k^{k_f}\right)_+ - \overline{u}_{k_f}^n\left(\mathscr{F}_f^n(\phi_\star^{n+1})\cdot\mathfrak{n}_k^{k_f}\right)_-\right)\mathfrak{m}_f \end{aligned} \tag{3.4}$$

with the positive and negative part functions defined by $(\psi)_\pm := \frac{|\psi|\pm\psi}{2}$.

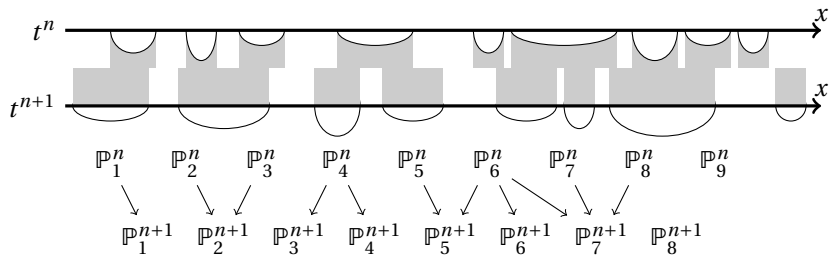


FIG. 3. *Definition of the graph of connections from the pocket supports. The top figure is an example of pockets at two successive time steps with the support of each pocket in gray. The figure below is the corresponding graph of connection.*

The numerical scheme (3.3) and (3.4) is first order in time and space. As stated in [31, Theorem 2.3], it is entropy-stable under the condition $\kappa \geq 1$ and the implicit CFL condition

$$\delta_t^{n+1} \leq \frac{\min\left(\delta_k, \delta_{k_f}\right) \min\left(h_k^{n+1}, h_{k_f}^{n+1}\right)}{2\left(\left(h^{n+1}\overline{u}^n\right)_f \cdot \mathfrak{n}_k^{k_f} + \left(h^{n+1}\right)_f \sqrt{\frac{\kappa}{2}\left|\left[\phi^{n+1}\right]_k^{k_f}\right|}\right)}. \tag{3.5}$$

**3.2. Numerical scheme of the pockets dynamics.** The current section is devoted to the main novelty of the paper, namely the pressure dynamics in air pockets. First, in §3.2.1, we propose a strategy to identify the likely connection between pockets at time $t^n$ and time $t^{n+1}$ based on the pocket supports. Then, in §3.2.2, we solve the problem of the evolution of the pressure inside the air pocket during a time step. Finally, to avoid numerical instabilities, a regularization of the air pressure in the congested areas is necessary and is detailed in the §3.2.4.

**3.2.1. Identification and connectivity of the pockets.** The discrete support of the pockets (discrete counterpart of $\Omega_i\left(\overline{h}\right)$) is defined by $\mathbb{P}_i^n = \left\{k \in \mathbb{T} \mid h_k^n < \overline{H}_k^n\right\}$ such that $\left(\mathbb{P}_i^n, \bigcup_{k\in\mathbb{P}_i^n} \mathbb{F}_k\right)$ is a connected graph. We use here the set of faces $f \in \mathbb{F}_k$ as the connectivity between $k$ and its neighbor $k_f$. We define all pockets in this way, which means that for any $k \in \mathbb{T}$ such that $h_k^n < \overline{H}_k^n$, there exists $i$ such that $k \in \mathbb{P}_i^n$ and for any $i \mathfrak{n} j$ we have $\mathbb{P}_i^n \cap \mathbb{P}_j^n = \emptyset$. The number of pockets is $N_p^n = \text{card}\left\{\mathbb{P}_i^n\right\}$ and for simplicity, we assume that the indices of the pockets are numbered from 1 to $N_p^n$. The discrete counterpart of the volume (2.5) is simply written

$$V_i^n = \sum_{k\in\mathbb{P}_i^n} \left(\overline{H}_k^n - h_k^n\right) \mathfrak{m}_k.$$

Once the water depth $h_k^{n+1}$ is computed using (3.3), it is possible to define the pockets $\mathbb{P}_{1\leq i\leq N_p^{n+1}}^{n+1}$ and the volume $V_{1\leq i\leq N_p^{n+1}}^{n+1}$. Nevertheless, the information we have is only pictures of the pockets at time $t^n$ and $t^{n+1}$. We are missing important information in the evolution of the pockets, in particular, which pockets at time $t^n$ led to which pockets at time $t^{n+1}$, with or without splitting and merging and at which time $t^*$. This is a classical problem of optimal transport [32]. However, optimal transport algorithms require a non-negligible numerical cost, especially in a two-dimensional setting.

We propose an alternative strategy based on pocket supports. More precisely, if there

exist a control volume $k$ shared by two pockets $\mathbb{P}_i^n$ and $\mathbb{P}_j^{n+1}$, we assume that the two pockets are connected, namely

$$\underline{\mathbb{L}}_i^{n+1} = \left\{1 \le j \le N_p^{n+1} \mid \mathbb{P}_i^n \cap \mathbb{P}_j^{n+1} \neq \varnothing\right\} \quad \text{and} \quad \overline{\mathbb{L}}_j^{n+1} = \left\{1 \le i \le N_p^n \mid \mathbb{P}_i^n \cap \mathbb{P}_j^{n+1} \neq \varnothing\right\}.$$

We obtained a bipartite graph $\left(\left\{\left[1, N_p^n\right] \cap \mathbb{N}, \left[1, N_p^{n+1}\right] \cap \mathbb{N}\right\}, \underline{\mathbb{L}}_{1\le i\le N_p^n}^{n+1}, \overline{\mathbb{L}}_{1\le j\le N_p^{n+1}}^{n+1}\right)$ between the pockets at time $t^n$ and the pockets at time $t^{n+1}$, see Fig. 3. To simplify the problem, we note that it can be divided into independent subproblems corresponding to the connected subgraphs. More precisely, we define $\overline{A}_l^{n+1} \subset \left[1, N_p^n\right] \cap \mathbb{N}$ the set of initial pockets and $\underline{A}_l^{n+1} \subset \left[1, N_p^{n+1}\right] \cap \mathbb{N}$ the set of resulting pockets of the $l^{th}$ independent sub-problem by

$$\overline{A}_l^{n+1} = \bigcup_{j\in\underline{A}_l^{n+1}} \overline{\mathbb{L}}_j^{n+1} \qquad \text{and} \qquad \underline{A}_l^{n+1} = \bigcup_{i\in\overline{A}_l^{n+1}} \underline{\mathbb{L}}_i^{n+1} \tag{3.6}$$

such that $\left(\left\{\overline{A}_l^{n+1}, \underline{A}_l^{n+1}\right\}, \underline{\mathbb{L}}_{\overline{A}_l^{n+1}}^{n+1}, \overline{\mathbb{L}}_{\underline{A}_l^{n+1}}^{n+1}\right)$ is connected, with $\underline{\mathbb{L}}_{\overline{A}_l^{n+1}}^{n+1} = \left\{\underline{\mathbb{L}}_i^{n+1} \mid i \in \overline{A}_l^{n+1}\right\}$ and $\overline{\mathbb{L}}_{\underline{A}_l^{n+1}}^{n+1} = \left\{\overline{\mathbb{L}}_j^{n+1} \mid j \in \underline{A}_l^{n+1}\right\}$. The number $M^{n+1}$ of independent subproblems is such that all pockets are considered, i.e. $\bigcup_{l=1}^{M^{n+1}} \overline{A}_l^{n+1} = \left[1, N_p^n\right] \cap \mathbb{N}$ and $\bigcup_{l=1}^{M^{n+1}} \underline{A}_l^{n+1} = \left[1, N_p^{n+1}\right] \cap \mathbb{N}$.

To illustrate our definitions, we detail the case drawn in Fig. 3. There are 6 independent subproblems, which we describe from left to right.

- The first subproblem corresponds to the graph $(\{\{1\},\{1\}\},\{\{1\}\},\{\{1\}\})$ is a simple deformation of the pocket.
- The second sub-problem $(\{\{2,3\},\{2\}\},\{\{2\},\{2\}\},\{\{2,3\}\})$ corresponds to the merging of two pockets. The pockets are also deformed, so it is not a simple application of (2.7).
- The third subproblem $(\{\{4\},\{3,4\}\},\{\{3,4\}\},\{\{3\},\{4\}\})$ corresponds to the splitting into two pockets. The pockets are also deformed, so it is not a simple application of (2.6).
- The fourth sub-problem $(\{\{5,6,7,8\},\{5,6,7\}\},\{\{5\},\{5,6,7\},\{7\},\{7\}\},\{\{5,6\},\{6\},\{6,7,8\}\})$ illustrates the fact that a pocket can be both split and merged during a time step, here the pocket $\mathbb{P}_6^n$.
- The last two subproblems $(\{\{9\},\{\}\},\{\{\}\},\{\}\})$ and $(\{\{\},\{8\}\},\{\},\{\{\}\})$ correspond to the two particular cases where a pocket disappears or respectively appears. These two cases required a particular treatment which will be explained in §3.2.3.

In practice, because of the small time step, there are never a large number of pockets involved in each sub-problem.

**3.2.2. Evolution of the pressure values along a time step.** In this section, we focus on solving a general pocket problem in interactions where we have removed the superscript of time and of the subproblem number $^{n+1}_{l}$ for readability reasons. The problem can be formulated as follows:

*Knowing the bipartite graph of interactions* $\left(\left\{\overline{A}, \underline{A}\right\}, \underline{\mathbb{L}}_{\overline{A}}, \overline{\mathbb{L}}_{\underline{A}}\right)$*, the volume* $V_{i\in\overline{A}}^n$ *and pressure* $P_{i\in\overline{A}}^n$ *of the initial pockets, and the volumes* $V_{j\in\underline{A}}^{n+1}$ *of the resulting pockets, find the pressures* $P_{j\in\underline{A}}^{n+1}$ *in the resulting pockets following the physical processes* (2.8)*,* (2.6) *and* (2.7)*.*

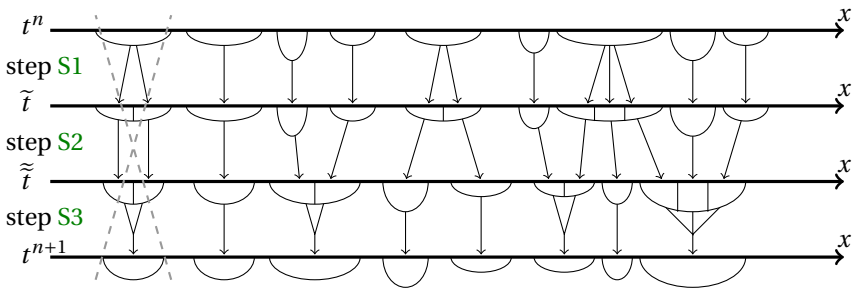


FIG. 4. *Illustration of the sub-steps of the pressure evolution scheme. From left to right: Unaccepted splitting/merging rejected by Hypothesis 1, typical deforming case, typical splitting case, typical merging case and complexe case (corresponding to the fourth case of Fig. 3).*

This problem is clearly ill-posed without additional assumptions. In particular because the splitting/merging times are unknown. We assume that the dynamics of the pockets during each time step can be divided into three steps, see Fig. 4.

S1 **Splitting step:** The splitting only occurs at the beginning of the time step. It satisfies (2.6) with $t^* = t^n$. Hence for any $i \in \overline{A}$ we have

$$\sum_{j \in \underline{\mathbb{L}}_i} \widetilde{V}_{ij} = V_i^n \qquad \text{and for any } j \in \underline{\mathbb{L}}_i, \quad \widetilde{P}_{ij} \widetilde{V}_{ij}^s = P_i^n \left(V_i^n\right)^s$$

with $\widetilde{V}_{ij}$ and $\widetilde{P}_{ij}$ respectively the volume and the pressure in the pocket after splitting and before deforming.

S2 **Deforming step:** The deformation without splitting or merging occurs during the time step. It satisfies (2.8). Hence for any $i \in \overline{A}$ and $j \in \underline{\mathbb{L}}_i$ we have

$$\widetilde{\widetilde{P}}_{ij} \widetilde{\widetilde{V}}_{ij}^d = \widetilde{P}_{ij} \widetilde{V}_{ij}^d.$$

with $\widetilde{\widetilde{V}}_{ij}$ and $\widetilde{\widetilde{P}}_{ij}$ respectively the volume and the pressure in the pocket after deforming and before merging.

S3 **Merging step:** The merging only occurs at the end of the time step. It satisfies (2.7) with $t^* = t^{n+1}$. Hence for any $j \in \underline{A}$ we have

$$\left(P_j^{n+1}\right)^{\frac{1}{m}} V_j^{n+1} = \sum_{i \in \overline{\mathbb{L}}_j} \left(\widetilde{\widetilde{P}}_{ij}\right)^{\frac{1}{m}} \widetilde{\widetilde{V}}_{ij} \qquad \text{and} \qquad V_j^{n+1} = \sum_{i \in \overline{\mathbb{L}}_j} \widetilde{\widetilde{V}}_{ij}.$$

The connectivity defined in §3.2.1 is not sufficient to conclude the pocket dynamics with the three steps S1, S2 and S3. For example, if we consider a single initial pocket connected to a single resulting pocket, it is possible, without further assumptions, that during the time step the pocket is first divided, each part is deformed separately and then merged to form the new pocket. This problem is illustrated by the first two cases of Fig. 4. To resolve this indeterminacy, we assume in what follows that the minimum required split/merge occurs.

HYPOTHESIS 1. *Each pocket $i \in \overline{A}$ is split exactly into* $\operatorname{card} \underline{\mathbb{L}}_i$ *pockets.*

Another missing information is the position where the pocket is split, or conversely the position where the pockets will merge. For example, from a single initial pocket that splits into two resulting pockets of equal volume, it is possible that the split occurs in the

middle, resulting in a similar deformation for the two new pockets, but it is also possible that the separation occurs at a third, and that the first pocket extends twice as much as the second. Instead of assuming the location of the split, which can lead to significant error for large pockets, we assume that all pockets resulting from the split are deformed proportionally. Since this assumption holds only for the time step where the split occurs, we expect a smaller impact on the outcome. The same problem arises when merging.

HYPOTHESIS 2.

*i) All the pockets resulting from the split of the same initial pocket grow globally in a proportional way, i.e. for any $i \in \overline{A}$, there exists $\widetilde{\Gamma}_i$ such that for any $j \in \underline{\mathbb{L}}_i$ one has*

$$\widetilde{V}_{ij} = \widetilde{\Gamma}_i \widetilde{\widetilde{V}}_{ij}.$$

*ii) All pockets participating in the merge of the same resulting pocket grow globally in a proportional way, i.e. for any $j \in \underline{A}$, there exists $\widetilde{\widetilde{\Gamma}}_j$ such that for any $i \in \overline{\mathbb{L}}_j$ one has*

$$\widetilde{V}_{ij} = \widetilde{\widetilde{\Gamma}}_j \widetilde{\widetilde{V}}_{ij}.$$

Also by construction, the graph satisfies the following assumption, see §3.2.1.

HYPOTHESIS 3. *The graph $\left(\left\{\overline{A}, \underline{A}\right\}, \underline{\mathbb{L}}_{\overline{A}}, \overline{\mathbb{L}}_{\underline{A}}\right)$ is connected and satisfies the relation*

$$\overline{A} = \bigcup_{j \in \underline{A}} \overline{\mathbb{L}}_j \qquad \text{and} \qquad \underline{A} = \bigcup_{i \in \overline{A}} \underline{\mathbb{L}}_i.$$

To conclude, the following assumption is necessary.

HYPOTHESIS 4. *The graph $\left(\left\{\overline{A}, \underline{A}\right\}, \underline{\mathbb{L}}_{\overline{A}}, \overline{\mathbb{L}}_{\underline{A}}\right)$ is acyclic, i.e. it contains no cycles.*

We are now able to solve the stated problem.

PROPOSITION 1. *Assume that the graph $\left(\left\{\overline{A}, \underline{A}\right\}, \underline{\mathbb{L}}_{\overline{A}}, \overline{\mathbb{L}}_{\underline{A}}\right)$ with $\operatorname{card} \overline{A} > 0$ and $\operatorname{card} \underline{A} > 0$ satisfies Hypothesis 3 and 4, and the evolution of the pockets follows the three steps S1, S2 and S3 and satisfies Hypothesis 1 and 2. Then for any $V^n_{i\in\overline{A}} > 0, P^n_{i\in\overline{A}}$ and $V^{n+1}_{j\in\underline{A}} > 0$, the pressures in the pockets $P^{n+1}_{j\in\underline{A}}$ are well-defined and given for any $j \in \underline{A}$ by*

$$P_j^{n+1} = \frac{\Gamma^{d-m}}{\left(V_j^{n+1}\right)^m} \left( \sum_{i \in \overline{\mathbb{L}}_j} \left( P_{ij} V_{ij}^s \widetilde{V}_{ij}^{m-s} \right)^{\frac{1}{m}} \right)^m \qquad \text{with} \qquad \Gamma = \frac{\sum_{i\in\overline{A}} V_i^n}{\sum_{j\in\underline{A}} V_j^{n+1}} \tag{3.7}$$

*and $\widetilde{V}_{ij}$ is the solution of the (well-posed) linear system*

$$\begin{aligned} &\text{for any } i \in \overline{A}\,, \quad \sum_{j \in \underline{\mathbb{L}}_i} \widetilde{V}_{ij} = V_i^n \\ &\text{for any } j \in \underline{A}\,, \quad \sum_{i \in \overline{\mathbb{L}}_j} \widetilde{V}_{ij} = \Gamma V_j^{n+1}. \end{aligned} \tag{3.8}$$

*Proof.* Using Hypothesis 3, for a given $i$ and for all $j \in \underline{\mathbb{L}}_i$ we also have $i \in \overline{\mathbb{L}}_j$. Using Hypothesis 2.i) and ii), we conclude that $\widetilde{\Gamma}_i = \widetilde{\widetilde{\Gamma}}_j$. By convexity of the graph (Hypothesis 3), we conclude that all the constants $\widetilde{\Gamma}_i$ and $\widetilde{\widetilde{\Gamma}}_j$ are the same, which we will write from now on $\Gamma$. Also the set of connections can be browsed either for all $i \in \overline{A}$ considering all $j \in \underline{\mathbb{L}}_i$,

or for all $j \in \underline{A}$ considering all $i \in \overline{\mathbb{L}}_j$. Adding up all the connections and using the volume conservation during the steps S1 and S3, we get

$$\sum_{i\in\overline{A}} V_i^n \overset{(S1)}{=} \sum_{i\in\overline{A}}\sum_{j\in\underline{\mathbb{L}}_i} \widetilde{V}_{ij} \overset{(H2)}{=} \Gamma \sum_{j\in\underline{A}}\sum_{i\in\overline{\mathbb{L}}_j} \widetilde{\widetilde{V}}_{ij} \overset{(S3)}{=} \Gamma \sum_{j\in\underline{A}} V_j^{n+1}.$$

Now using the polytropic formulae of each step S1, S2 and S3, we write

$$\begin{aligned}\left(P_j^{n+1}\right)^{\frac{1}{m}} V_j^{n+1} &\overset{(S3)}{=} \sum_{i\in\overline{\mathbb{L}}_j} \widetilde{\widetilde{P}}_{ij}^{\frac{1}{m}} \widetilde{\widetilde{V}}_{ij} \overset{(S2)}{=} \sum_{i\in\overline{\mathbb{L}}_j} \left(\widetilde{P}_{ij}\widetilde{V}_{ij}^d \widetilde{\widetilde{V}}_{ij}^{m-d}\right)^{\frac{1}{m}} \\ &\overset{(H2)}{=} \Gamma^{\frac{m-d}{m}} \sum_{i\in\overline{\mathbb{L}}_j} \left(\widetilde{P}_{ij}\widetilde{V}_{ij}^m\right)^{\frac{1}{m}} \overset{(S1)}{=} \Gamma^{\frac{m-d}{m}} \sum_{i\in\overline{\mathbb{L}}_j} \left(P_{ij}V_{ij}^s \widetilde{V}_{ij}^{m-s}\right)^{\frac{1}{m}}.\end{aligned}$$

It remains to estimate the volumes $\widetilde{V}_{ij}$. The linear system (3.8) is nothing else than the volume conservation of the steps S1 and S3 using $\widetilde{\Gamma}_i = \widetilde{\widetilde{\Gamma}}_j = \Gamma$. Thanks to Hypothesis 3 and 4, the graph $\left(\left\{\overline{A}, \underline{A}\right\}, \underline{\mathbb{L}}_{\overline{A}}, \overline{\mathbb{L}}_{\underline{A}}\right)$ is a tree. Hence the number of vertices $\operatorname{card}\overline{A} + \operatorname{card}\underline{A}$ is greater by one than the number of edges $\sum_{i\in\overline{A}} \operatorname{card}\underline{\mathbb{L}}_i$. We conclude that there is one more equation than unknowns in (3.8). However, by adding the first equations for $i \in \overline{A}$ and the last one for $j \in \underline{A}$, we recover the definition of $\Gamma$. This means that an equation (any one) can be deleted without loss of information. Since the graph is connected (Hypothesis 3), this means that the vectors defined by the coefficients of each row of the linear system (3.8) is a spanning set. We conclude that the (3.8) is well posed. ∎

REMARK 1. *In a one-dimensional framework ($D = 1$), the Hypothesis 4 holds by construction. In larger dimensional framework ($D > 1$), since Hypothesis 3 is always satisfied, it is easier to check the algebraic relation*

$$\operatorname{card}\overline{A} + \operatorname{card}\underline{A} - 1 = \sum_{i\in\overline{A}} \operatorname{card}\underline{\mathbb{L}}_i \tag{3.9}$$

*that ensure that Hypothesis 4 holds. If not, see §4.*

REMARK 2. *The system (3.8) is composed of a Boolean matrix. Therefore, it can be written as a lower triangular matrix by simply renumbering the unknowns and solved it by simple differences without the use of complexe linear algebra. Therefore, it can be written as a lower triangular matrix by simply renumbering the unknowns and can be solved by simple line differences without using complex linear algebra. However, there is no guarantee that the solution of this system is positive, which means that the pressures calculated by (3.7) may be unphysical negative values. See §4, in this case.*

**3.2.3. Particular cases of appearing and disappearing pockets.** It remains to treat the two particular cases of pockets that appear and disappear. These cases can occur physically if a vacuum (zero pressure) forms or collapses. The Torricelli's experiment (1644) is a historical proof. However, due to the weak coupling proposed in this work, non-physical pockets appearing and disappearing may occur.

In the case of a disappearing pocket ($\operatorname{card}\underline{A} = 0$), it is possible to know if the disappearance is physical or not, by looking at the pressure before the disappearance. If $P_i^n = 0$, there is no matter in the pocket and it can collapse, otherwise there is matter so the disappearance is non physical. Except in the case of isobaric deformation ($d = 0$), before collapse, the pressure should become very high and create a force opposing the collapse.

In the case of an appearing pocket ($\operatorname{card}\overline{A} = 0$), assuming the formation of the physical vacuum, we set the pressure inside to zero $P_i^{n+1} = 0$. If the vacuum formation is not

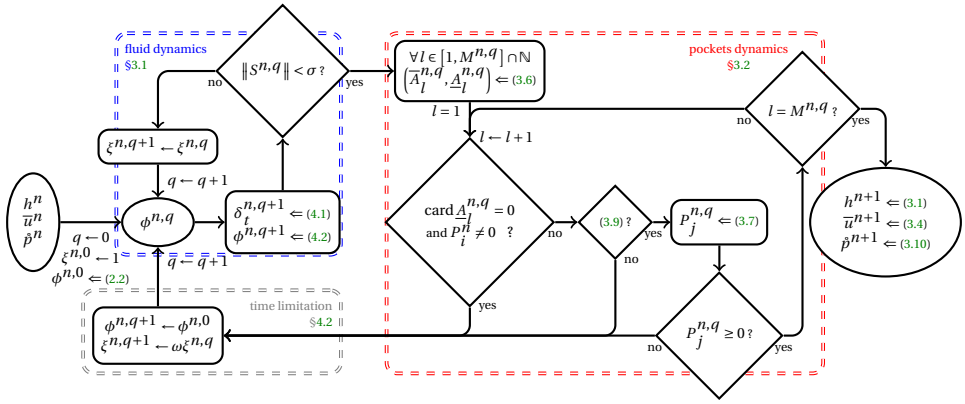


FIG. 5. *Flowchart of iterative processes of weak coupling. The space index has been removed for easier reading. The notation $a \leftarrow b$ is the numerical assignment, i.e. $a$ takes the value of $b$. The notation $a \Leftarrow (X)$ means that $a$ is computed using the equation (X).*

physical, the pocket will quickly collapse and the numerical strategy seems robust enough to handle it, see §5.2.

The numerical treatment of all these particular cases is discussed in §4.

**3.2.4. Regularization of the air pressure in the congested regions.** It remains to define the air pressure in the congested areas. A trivial counterpart of (2.4) should be to set the air pressure to zero in congested areas. Nevertheless, due to the weak coupling, this solution leads to instabilities at the waterline. An Air pressure regularization is necessary. Since the roof reaction is non-negative, see (2.3), the regularization support should not be too large to prevent water from coming off the roof because of it. More precisely, the discrete counterpart of (2.4) reads

$$\mathring{p}_k^{n+1} = \max\left(0, \left(1 - \left|\frac{\mathfrak{D}_{\mathbb{P}_i^{n+1}}(k)}{\overline{\mathfrak{D}}}\right|^2\right) P_i^{n+1}\right) \tag{3.10}$$

with $i$ such that $\mathfrak{D}_{\mathbb{P}_i^{n+1}}(k) = \min_{1\le j\le N_p^{n+1}} \mathfrak{D}_{\mathbb{P}_j^{n+1}}(k)$, where $\mathfrak{D}_{\mathbb{P}_j}(k)$ is the distance of the mass center of the $k^{th}$ control volume to the pocket $\mathbb{P}_j$ and $\overline{\mathfrak{D}} > 0$ is a given distance characteristic of the regularization. The choice of the regularization profile is arbitrary, although several profiles have been tried and the second order polynomial seems to be well suited.

## 4. Pratical implementation.

**4.1. Description of the time step computation.** Several points need to be clarified in solving the scheme (3.3), (3.4), (3.7) and (3.10) in practice. First, the fluid dynamics scheme §3.1 is an ImEx (implicit explicit) nonlinear scheme and requires a fixed point algorithm to solve. Second, the pocket dynamics §3.2 has a number of special cases and we use this section to clarify how the algorithm handles them. A flowchart of the algorithm is drawn in Fig. 5 to illustrate it.

Starting from the approximation of the state variables at time $t^n$, i.e. $h_\star^n$, $\overline{u}_\star^n$ and $\mathring{p}_\star^n$, we start by estimating the new potential using a Newton fixed point already presented in [31]. A first estimate of the potential is given by $\phi_k^{n,0} = \phi\left(h_k^n, g\rho\frac{\left(h_k^n - \overline{H}_k^n\right)_+}{\lambda_k^2}, \mathring{p}_k^n, B_k^n\right)$ with the

function defined by (2.2). The time step is estimate to satisfy the implicit CFL condition (3.5) at convergence

$$\delta_t^{n,q+1} = \min\left(\delta_t^{n,q}, \min_{f\in\mathbb{F}}\left(\frac{\xi^{n,q}\min\left(\delta_k,\delta_{k_f}\right)\min\left(h_k^{n,q},h_{k_f}^{n,q}\right)}{2\left(\left(h^{n,q}\overline{u}^n\right)_f\cdot\mathfrak{n}_k^{k_f}+\left(h^{n,q}\right)_f\sqrt{\frac{\kappa}{2}\left|\left[\phi^{n,q}\right]_k^{k_f}\right|}\right)}\right)\right) \tag{4.1}$$

where $q$ is the index of the Newton fixed point and $h_k^{n,q}=\mathscr{H}_k^n\left(\phi_k^{n,q}\right)$ and $\mathbb{F}=\cup_{k\in\mathbb{T}}\mathbb{F}_k$ is the set of faces of the mesh and $0<\xi^{n,q}\leq 1$ is an adaptive CFL parameter, see §4.2, initialized by $\xi^{n,0}=1$. Using this time step, we compute an new approximation of the potential $\phi_\star^{n,q+1}$ thanks to

$$J^{n,q}\left(\phi_\star^{n,q}\right)\widetilde{\phi}_\star^{n,q+1}=S_\star^{n,q}\left(\phi_\star^{n,q}\right)\qquad\text{and}\qquad\phi_\star^{n,q+1}=\phi_\star^{n,q}-\widetilde{\phi}_\star^{n,q+1} \tag{4.2}$$

with $J^{n,q}\left(\phi_\star\right)$ is the Jacobian of the residual $S_\star^{n,q}\left(\phi_\star\right)$ defined by (3.3). This process (time step estimation and potential computation) is iterated until convergence. In the present work, we consider that the fixed point is converged if the $L^\infty$-norm of the residual $S_\star^{n,q}\left(\phi_\star^{n,q}\right)$ is less than a tolerance $\sigma>0$ and in practice less than 10 iterations are needed with $\sigma=10^{-10}$.

At convergence, the pockets are identified from the last approximation of the water depth $h^{n,q+1}$, see §3.2.1, and divided into $M^{n,q}$ subproblems corresponding to the graphs $\left(\left\{\overline{A}_l^{n,q},\underline{A}_l^{n,q}\right\},\mathbb{L}_{\overline{A}_l^{n,q}}^{n,q},\mathbb{L}_{\underline{A}_l^{n,q}}^{n,q}\right)$. For each connected group of pockets $1\leq l\leq M^{n,q}$ (which can be treated in parallel), we first check if it corresponds to a pocket which disappears with a non-zero pressure, i.e. $\operatorname{card}\underline{A}_l^{n,q}=0$ with $P_{i\in\overline{A}_l^{n,q}}^{n,q}\neq 0$, see §3.2.2. In this case, the time step is reduced to avoid it, see §4.2. Then we test if the pockets appear, i.e. $\operatorname{card}\overline{A}_l^{n,q}=0$, in which case we put $P_{j\in\overline{A}_l^{n,q}}=0$, see §3.2.2. Otherwise, before computing the pressure, we check (except in a one-dimensional framework) if the problem is well posed by testing (3.9), see Remark 1. If the graph has a cycle, we cannot compute the pressure, the time step is reduced to reduce the number of interactions, see §4.2. However, as there is no guarantee that the pressure is non-negative, see Remark 2, we check a posteriori for non-negativity. If one of the new pressures is negative, we reduce the time step here too, see §4.2. Once the new pressures $P_{1\leq j\leq N_p^{n,q}}^{n,q}$ are known in each pocket, the time step is completed by setting the water depth $h_k^{n+1}=\mathscr{H}_k^n\left(\phi_k^{n,q+1}\right)$ with (3.1), the velocity $\overline{u}_k^{n+1}$ using (3.4) and the air pressure $\mathring{p}_k^{n+1}$ using (3.10).

**4.2. Time step limiting process with adaptive CFL parameter.** As explained in §4.1, there are situations where the problem is ill-posed and a time step limitation is necessary. In these cases, we reduce the adaptive parameterization $\xi^{n,q+1}=\omega\xi^{n,q}$ with a given limiting factor $0<\omega<1$. The potential is also reset by setting $\phi_k^{n,q+1}=\phi\left(h_k^n,g\rho\frac{\left(h_k^n-\overline{H}_k^n\right)_+}{\lambda_k^2},\mathring{p}_k^n,B_k^n\right)$ and Newton's fixed point is stated again, see Fig. 5.

**4.3. Discrete boundary conditions.** As explained in §2.4, we assume that the flow at the boundary is not congested, so the shallow water model boundary condition can be used. For any cell $i\in\mathbb{T}$ with a face on the boundary $\mathbb{F}_i\cap\partial\mathbb{T}\neq 0$, we create a ghost cell $g$ with the same geometry, i.e. $\mathfrak{m}_g=\mathfrak{m}_i$. We consider two cases.

**wall boundary:** We assume that there is a wall at the boundary such that the flow in the ghost cell is symmetric to the flow inside, that is, $h_g^n=h_i^n$, $\overline{u}_g^n cdot\left(\mathfrak{n}_i^g\right)^\perp=\overline{u}_i^n cdot\left(\mathfrak{n}_i^g\right)^\perp$

and $\overline{u}_g^n cdot \mathfrak{n}_i^g = -\overline{u}_i^n cdot \mathfrak{n}_i^g$. The pressures in the pocket reaching only this type of border are computed as within the computational domain.

**open boundary:** We assume that the flow is across the boundary. Many strategies exist in the literature. We consider here only the case of a fixed water depth $h_g^n = H > 0$ and the velocity is computed thanks to the Riemann invariant, i.e. $\overline{u}_g^n \cdot \mathfrak{n}_i^g = \overline{u}_i^n \cdot \mathfrak{n}_i^g + 2\sqrt{gh_i^n} - 2\sqrt{gH}$. The last component is set to zero, i.e. $\overline{u}_g^n \cdot \left(\mathfrak{n}_i^g\right)^\perp = 0$. Anyway, for all pockets that reach this type of boundary, we impose the inside pressure. For all pockets that reach this type of border, we impose the inner pressure.

**5. Numerical evidences.** The present section is devoted to some numerical illustrations in a one-dimensional framework ($D = 1$) of the numerical strategy (3.3), (3.4), (3.7) and (3.10). For all the simulations, a regular mesh is used, i.e. for any $k \in \mathbb{T}$ we have $\delta_k = \delta_x$. We start with the simulation of the stationary states of the model §5.1 to illustrate the well balanced property of the scheme. Then we reproduce the historical experiment of Torricelli §5.2. In these two cases, the dynamics of the air pockets do not appear, due to the equilibrium for the former and the vacuum for the latter. Then we numerically study the influence of the polytropic parameters of deformation §5.3 and of melting §5.4. A non-isobaric splitting does not seem physically relevant, so it is not studied in this work. Finally, we propose a more concrete illustration by the flooding of a coastal cave during the rise of water and the impact on the pressure inside due to wave forcing §5.5. Unless otherwise specified, the physical parameters, i.e. acceleration of gravity, density of the fluid, polytropic parameters and the computational domain are fixed at

$$g = 9.81\,, \qquad \rho = 10^3\,, \qquad s = 0\,, \qquad d = 1\,, \qquad m = 1.4 \qquad \text{and} \qquad \Omega = [0,1]\,. \tag{5.1}$$

Assuming the units are those of the International System of Units, the physical parameter values are approximately that of geophysical applications. Similarly, the initial pressure is set (unless specified) to $10^5$, which corresponds to $1atm$. The numerical parameters, i.e. penetration, regularization, CFL limiting factor, distance of regularization and Newton's fixed point tolerance are respectively set (unless specified) to

$$\lambda^2 = \delta_x\,, \qquad \kappa = 1\,, \qquad \omega = 0.5\,, \qquad \overline{\mathfrak{D}} = 10^{-2}. \qquad \text{and} \qquad \sigma = 10^{-10}. \tag{5.2}$$

**5.1. Steady states at rest.** This section is devoted to the steady state at rest of the model (2.1), (2.2), (2.3), (2.4), (2.5), (2.6), (2.7) and (2.8). For the congested shallow water model without air pocket modeling, the steady state at rest is defined by $\overline{u}(t,x) = 0$ and a constant $\Phi$ such that $\phi(t,x) = \Phi$ for all $(t,x) \in \mathbb{R}_+ \times \mathbb{R}$, see [20][1]. In the case of air pocket modeling, the potential $\Phi$ is not sufficient and the pressure in each pocket is also required, while the water depth can be deduced by

$$h(t,x) = \max\left(0, \min\left(\frac{\rho\Phi - \mathring{p}(t,x)}{g\rho}, R(t,x)\right) - B(t,x)\right)$$

where $\mathring{p}$ is deduce from $P_i$ and $h$ by (2.4). As for the initial condition, see §2.3, it is not trivial to define the steady state in general because of the link between the definition of the support of each pocket and the pressure.

Let us take an example. The bottom is set at

$$B(t,x) = 1.5e^{-\left|\frac{x-0.1}{0.05}\right|^2} + 2.5e^{-\left|\frac{x-0.3}{0.05}\right|^2} + 3e^{-\left|\frac{x-0.5}{0.05}\right|^2} + 2\mathbb{1}_{[0.6,0.8]}(x)$$

[1] The potential $\Phi$ is in fact constant per connected part of the support of $h$.

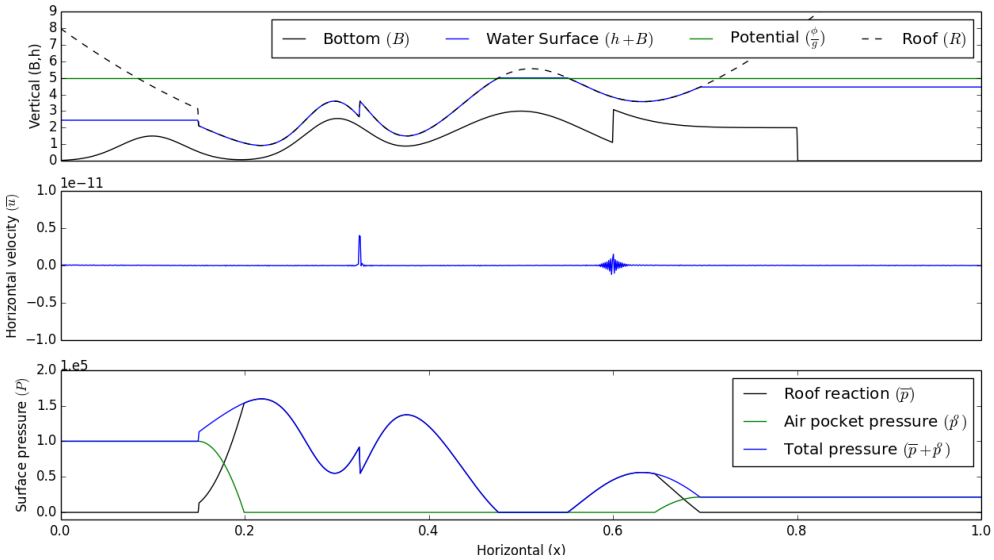


FIG. 6. *§5.1 Steady states at rest. Solution of the numerical strategy* (3.3), (3.4), (3.7) *and* (3.10) *initialized to the steady state after 100 time steps.*

and the roof is set at

$$R(t,x) = 50(x-0.4)^2 - \mathbb{1}_{[0.175,0.325]}(x) + 4e^{-\left|\frac{x-0.3}{0.05}\right|^2} + 5e^{-\left|\frac{x-0.5}{0.01}\right|^2}.$$

We consider three air pockets with the respective pressure from left to right

$$P_1^0 = 10^5, \qquad P_2^0 = 0 \qquad \text{and} \qquad P_3^0 = P_1^0 - 2g\rho.$$

We set here $\Phi = 5g$ and $\rho = 4\cdot 10^3$. The bottom and the roof are defined in such a way that all possible cases are present, i.e. a continuous or discontinuous bottom and roof, especially at the waterline. In this test case, we use wall boundary conditions. The other parameters are given by (5.1) and (5.2).

At the discrete level, the steady state is not the cell average of the continuous steady state, in part because of the pressure regularization (3.10). In practice, to initialize to the steady state at rest, we define an approximation of the water depth $\overline{h}_k^0 = h(0,x_k)$ with $x_k$ the center of mass of the cell. This approximation coincides with the discrete steady state in the non-congested areas; thanks to it, we can define the support of the air pockets, and then the atmospheric pressure $\mathring{p}_k^0$ using §3.10. Finally, the water depth is initialized using the function (3.1) by $h_k^0 = \mathscr{H}_k^0(\Phi)$.

To illustrate the well balanced property of the scheme, we plot in Fig. 6 at time $t = 1$ with $\delta_x = 10^{-3}$, $\delta_t = 10^{-2}$ and $\overline{\mathfrak{D}} = 5\cdot 10^{-2}$. The time step $\delta_t$ and the regularization distance $\overline{\mathfrak{D}}$ are artificially increased to obtain a better illustration. After 100 time steps, the steady state is preserved up to the machine error, as can be clearly seen in the horizontal velocity, although the error is larger at roof or bottom discontinuities in congested areas.

**5.2. Torricelli's experiment.** This section is devoted to the numerical realization of the Torricelli's experiment. We consider a piston with the open part emerged and initially at its lowest position. During the experiment, the piston gradually rises to a level where a

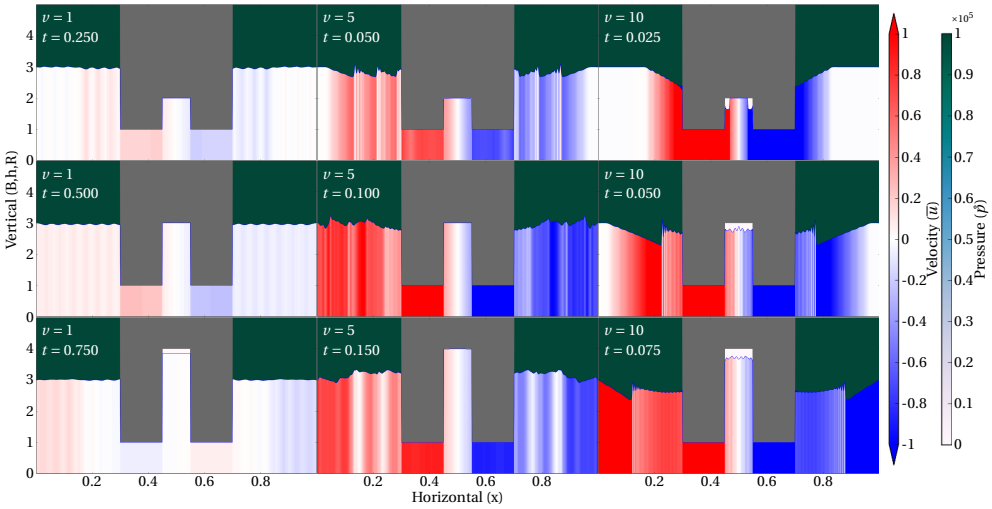


FIG. 7. *§5.2 Torricelli's experiment. Torricelli's experiments with different velocity of the piston (left column* $v = 1$*, middle column* $v = 5$*, right column* $v = 10$*) at several times (*$t = \frac{0.25l}{v}$ *where* $l$ *is the line number).*

vacuum pocket appears. We model this experiment using a flat bottom $B(t,x) = 0$ and the following roof function

$$R(t,x) = 5 - 4\left(\mathbb{1}_{[0.3,0.7]}(x) + vt\mathbb{1}_{[0.45,0.55]}(x)\right)$$

where $v$ is the velocity of the piston. The water is initially at rest $\overline{u}^0(x) = 0$ and $h^0(x) = \min\left(4, \overline{H}(0,x)\right)$. We use open boundary conditions with the water depth at the boundary set to $h(t,0) = h(t,1) = 4$ and the air pressure set to $10^5$. As for the historical experiment, we use $\rho = 13 \cdot 10^3$ (approximately the density of mercury). The other parameters are given by (5.1) and (5.2).

In Fig. 7, the numerical results with $\delta_x = 10^{-3}$ and several velocity of the piston (columns) are plotted at several times (lines). In the left column, the velocity of the piston is set to $v = 1$ and is slow enough that the fluid does not detach from the roof before time $t = 0.7$. At this time, the piston elevation is about 0.77 above the water surface, so the weight of the fluid inside is $10^5$. Then the water comes off of the roof and a vacuum pocket ($P = 0$) appears in the piston. In the central column, the velocity of the piston is fixed at $v = 5$. This velocity is high enough to create a pocket of vacuum at the beginning of the simulation, which quickly collapse. In the right column, the velocity of the piston is fixed at $v = 10$. We observe the same vacuum formation but in this case, the pocket does not collapse before several time steps, which seems to indicate that it does not come from a coupling artifice, but because of the inertia of the water. We observe two types of oscillations at the free surface and in the velocity. The small and fast oscillations appear to be spurious waves from the weak coupling strategy. They decrease in amplitude by using finer time steps. The larger oscillations with shock fronts are the reflection of the free surface reaching the roof inside the piston.

**5.3. Analysis of the polytropic coefficient of deformation.** While it can be assumed that deformations are isothermal when sufficiently slow, especially in groundwater applications, this is not necessarily the case for engineered devices such as marine energy

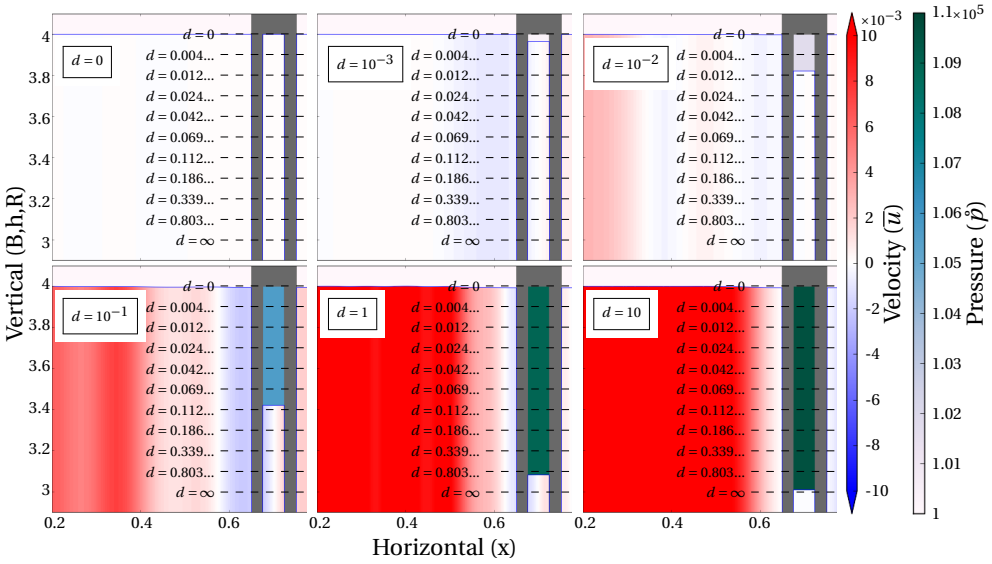


FIG. 8. *§5.3 Analysis of the polytropic coefficient of deformation. Compression of a pocket with different values of the polytropic coefficient of deformation. The dashed lines are graduations where the value of the polytropic coefficient is calculated with* (5.3).

converters. We propose a simple experiment to estimate the polytropic coefficient of deformation $d$. Consider a simple piston of uniform cross-section (rectangular or circular) initially having a position such that the elevation of the top of the piston above the fluid is $H_0$ and a pressure inside $P_0$. By lowering the piston by $H_0$ and waiting, we obtain a new steady state where we note $\widetilde{h}$ the height of the pocket in the piston. Assuming that the water level and pressure outside have not changed, we can deduce that the polytropic coefficient of deformation is

$$d = \frac{\log\left(1+\frac{g\rho\widetilde{h}}{P_0}\right)}{\log(H_0)-\log\left(\widetilde{h}\right)}. \tag{5.3}$$

Let us illustrate the experiment by reproducing it numerically. Let a flat bottom $B(t,x) = 0$ and a roof function given by

$$R(t,x) = 5 - 4\mathbb{1}_{[0.45,0.55]}(x) + (4-\min(t,1))\,\mathbb{1}_{[0.475,0.525]}(x)$$

The water is initially at rest $\overline{u}^0(x) = 0$ and $h^0(x) = \min\left(4, \overline{H}(0,x)\right)$. We use open boundary conditions with the water depth at the boundary set to $h(t,0) = h(t,1) = 4$ and the air pressure set to $10^5$. Except for the polytropic coefficient of deformation $d$ which depends on the simulations, the other parameters are given by (5.1) and (5.2).

In Fig. 8, the numerical results with $\delta_x = 2\cdot 10^{-3}$ and several polytropic coefficients of deformation are plotted at time $t = 2$. The top left image is calculated with $cd = 0$, i.e. an isobaric deformation. As expected, the pressure inside the piston remains unchanged and the water surface is not affected by the roof motion until it reaches the water surface. The other results are obtained with larger polytropic coefficients of deformation and are in good agreement with the theoretical values (5.3) plotted in dotted lines. The current

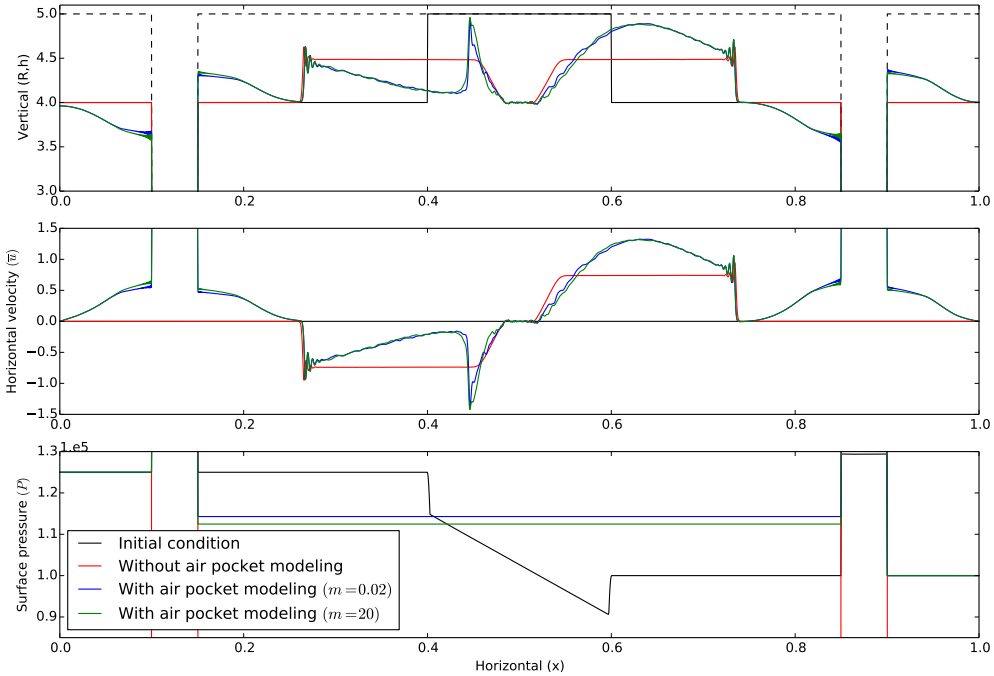


FIG. 9. *§5.4 Analysis of the polytropic coefficient of merging. Merging of two pockets with different values of the polytropic coefficient of merging (blue line $m = 0,02$, green line $m = 20$) at time $t = 2 \cdot 10^{-2}$.*

configuration is well suited to estimate $d \in \left[10^{-2}, 1\right]$. To estimate higher values, a lower initial pressure $P_0$ is preferred.

**5.4. Analysis of the polytropic coefficient of merging.** This section is devoted to the analysis of the polytropic coefficient of merging $m$. This parameter is quite difficult to determine in practice because the merger is a one-time event. However, we will see that this parameter has a small, almost negligible impact.

Let a flat bottom $B(t,x) = 0$ and a roof function given by

$$R(t,x) = 5 - 4\left(\mathbb{1}_{[0.1,0.9]}(x) - \mathbb{1}_{[0.15,0.85]}(x)\right).$$

Initially, the water is at rest and split the chamber into two pockets, namely

$$\overline{u}^0(x) = 0 \qquad \text{and} \qquad h^0(x) = 4 + \mathbb{1}_{[0.4,0.6]}(x).$$

To break the symmetry, the pressure in the air pockets is set to $P_1 = P_2 = 1.25 \cdot 10^5$ and $P_3 = P_4 = 10^5$. The initial condition is drawn in Fig. 9 by the solid black line. We use wall boundary conditions with the air pressure set to $10^5$. Except for the polytropic coefficient of merging $m$ which depends on the simulations, the other parameters are given by (5.1) and (5.2).

In Fig. 9, the solutions with $\delta_x = 5 \cdot 10^{-4}$ at time $t = 2 \cdot 10^{-2}$ with two values of the polytropic coefficient of merging are plotted (blue line $m = 0.02$, green line $m = 20$). The solution without air pressure modeling [20], is also plotted in red, of which we begin the description. The central water column falls, resulting in the formation of two shock waves, well known from shallow water modeling. The oscillations ahead of the shock waves are

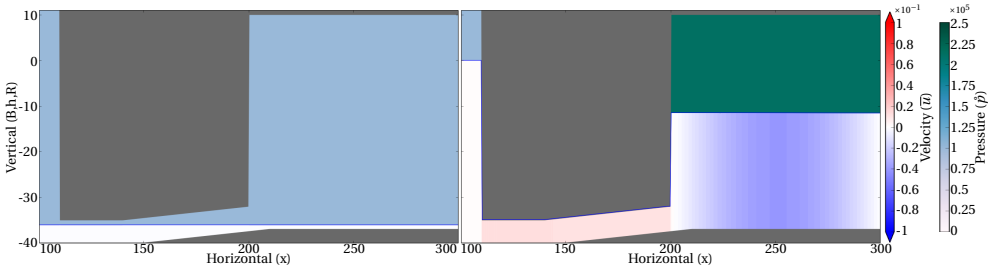


FIG. 10. *§5.5 Submerged cave. Rising water* (5.4). *Initial condition (left) and solution at time* $t = 4 \cdot 10^3$ *(right).*

artificial and due to the numerical dispersion of the CPR scheme [31]. When the entire water column has fallen, a new tray appears in the center.

Let us now describe the solutions with air pressure modeling, which are very similar despite the difference in the polytropic coefficient of merging. At the beginning of the simulation, i.e. before the two air pockets merge, the pressure difference breaks the symmetry by creating a lack of water in the high pressure pocket and an excess in the low pressure pocket. In addition, the deformation of each pocket changes the pressure inside, which causes a variation with the pressure outside the chamber, and then an exchange of water. When the two air pockets merge, the pressure is suddenly equalized but the water level is not. This creates a second wave from the pocket with the lowest pressure (and with the highest water level) to the pocket with the highest pressure (and with the lowest water level). We also remark that the air modeling does not significantly affect the shock waves, nor the final plateau in place of the initial water column. The air modeling does not significantly affect the shock waves, nor the final plateau in place of the initial water column. The oscillations at the waterline ($x = 0.1$, $x = 0.15$, $x = 0.85$ and $x = 0.9$) are due to the numerical dispersion of the CPR scheme, while the oscillations at the center ($x \in [0.3, 0.7]$) are mainly due to the weak coupling between air and water dynamics.

**5.5. Submerged cave.** The last test case is an illustration of a possible application of current work to geophysical studies. We propose a simulation of a conceptual coastal cave, as can be the Cosquer cave [14]. This test case can also be considered as an illustration of an oscillating water column marine energy converter [6].

Let the computational domain of $\Omega = [0, 300]$, the bottom and the roof being defined by

$$B(t,x) = -40 + \frac{\max(0, \min(x-150, 60))}{20} \qquad \text{and}$$
$$R(t,x) = 40 \mathbb{1}_{[0,10]}(x) + \left( \frac{\max(0, \min(x-140, 60))}{20} - 35 \right) \mathbb{1}_{[10,110]}(x) + 10 \mathbb{1}_{[210,300]}(x).$$

The right boundary condition is an wall and the left boundary condition is open, with the air pressure set to $10^5$.

We first consider a situation that mimics the sea level rise at the end of the ice age. Initially, the water is a lake at rest: $\overline{u}^0(x) = 0$ and $h^0(x) = -36 - B(0,x)$ and the air pressure is fixed by the boundary value. The water depth at the left boundary is defined by

$$h(t,0) = 4 + \min(0.01\, t, 36). \tag{5.4}$$

Fig. 10 shows the initial condition (left picture) and the solution at time $t = 4 \cdot 10^3$ (right

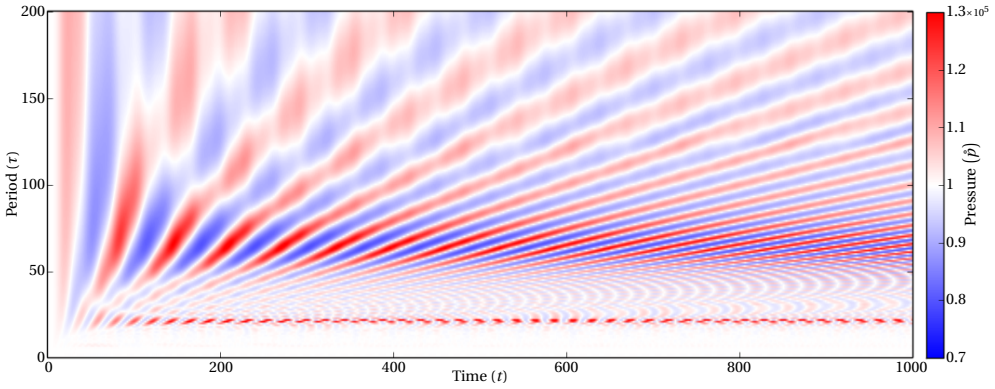


FIG. 11. *§5.5 Submerged cave. Wave impact* (5.5). *Pressure inside the cave during several wave periods.*

picture) with $\delta_x = 5 \cdot 10^{-1}$. As the water rises, an air pocket forms and compresses, resulting in higher pressure and a lower water level in the cave.

We then examine the impact of the tide or swell on the pressure in the cave. Initially, the water is a lake at rest $\overline{u}^0(x) = 0$ and $h^0(x) = -B(0,x)$ and the atmospheric pressure is fixed at $P_1^0 = P_2^0 = 10^5$. The water depth at the left boundary is defined by

$$h(t,0) = 40 + \cos\left(\frac{2\pi t}{\tau}\right) \tag{5.5}$$

Fig. 11 shows the time evolution of the pressure inside the cave for several values of the period $\tau$ simulated with $\delta_x = 2$. For small periods $\tau < 20$, the pressure is almost unchanged. The wavelength is smaller than the cave, so the volume of the pocket inside the cave remains unchanged. For a period around $\tau = 20$, the wavelength is close to the size of the cave. The water level inside the cave resonates with the waves, creating large pressure variations (almost exclusively overpressure). For periods $20 < \tau < 50$, the interactions with reflected waves are destructive and pressure variations remain relatively small. For long periods $50 < \tau < 70$, the water has time to rise in the cave between two waves creating an important pressure variation (overpressure and underpressure), with small dynamic effects amplifying the amplitude of the variations. For longer periods $\tau > 70$, the dynamic effects disappear and the amplitude of the pressure variations is constant. These results also depend on the geometry of the cave, especially the submerged part.

**6. Conclusion.** In this work, the modeling and numerical resolution in the multidimensional framework of the interaction between the congested shallow water model and a polytropic air pocket dynamics are addressed. A weak coupling strategy is adopted and the air pocket dynamics is assumed to satisfy several assumptions. These technical choices were made for efficiency reasons. However, in very specific situations, they can lead to irrelevant results such as a negative pressure or the disappearance of the air phase. In addition to these difficulties, the main lock of the current strategy lies in the dry front, prohibited by the CFL condition of the ImEx regime. Several other points can improve the physics of the model, are already covered in the literature and some strategies are directly compatible, for example the dynamics of a floating body [21], the dispersion terms [30] and the vertical variation of the horizontal velocity [2].

[1] ABGRALL, R., AND KARNI, S. Two-layer shallow water system: a relaxation approach. *SIAM J. Sci. Comput. 31* (2009), 1603–1627.
[2] AUDUSSE, E., BRISTEAU, M.-O., PERTHAME, B., AND SAINTE-MARIE, J. A multilayer Saint-Venant system with mass exchanges for shallow water flows. Derivation and numerical validation. *ESAIM: M2AN 45*, 1 (2011), 169–200.
[3] BERGMANN, M., HOVNANIAN, J., AND IOLLO, A. An accurate cartesian method for incompressible flows with moving boundaries. *Communications in Computational Physics 15*, 5 (2014), 1266–1290.
[4] BISPEN, G., LUKÁČOVÁ-MEDVID'OVÁ, M., AND YELASH, L. Asymptotic preserving imex finite volume schemes for low mach number euler equations with gravitation. *Journal of Computational Physics 335* (2017), 222–248.
[5] BOCCHI, E. Floating structures in shallow water: Local well-posedness in the axisymmetric case. *SIAM Journal on Mathematical Analysis 52*, 1 (2020), 306–339.
[6] BOCCHI, EDOARDO, HE, JIAO, AND VERGARA-HERMOSILLA, GASTÓN. Modelling and simulation of a wave energy converter. *ESAIM: ProcS 70* (2021), 68–83.
[7] BOSCHERI, W., DIMARCO, G., LOUBÈRE, R., TAVELLI, M., AND VIGNAL, M.-H. A second order all mach number imex finite volume solver for the three dimensional euler equations. *Journal of Computational Physics 415* (2020), 109486.
[8] BOSI, U., ENGSIG-KARUP, A. P., ESKILSSON, C., AND RICCHIUTO, M. A spectral/hp element depth-integrated model for nonlinear wave–body interaction. *Computer Methods in Applied Mechanics and Engineering 348* (2019), 222 – 249.
[9] BOURDARIAS, C., ERSOY, M., AND GERBI, S. Air entrainment in transient flows in closed water pipes : A two-layer approach. *ESAIM: M2AN 47*, 2 (2013), 507–538.
[10] BOURDARIAS, C., AND GERBI, S. A finite volume scheme for a model coupling free surface and pressurised flows in pipes. *Journal of Computational and Applied Mathematics 209*, 1 (2007), 109 – 131.
[11] BOYER, F. A theoretical and numerical model for the study of incompressible mixture flows. *Computers & Fluids 31*, 1 (2002), 41–68.
[12] ČERNE, G., PETELIN, S., AND TISELJ, I. Coupling of the interface tracking and the two-fluid models for the simulation of incompressible two-phase flow. *Journal of Computational Physics 171*, 2 (2001), 776–804.
[13] CHENG, L., RIBATSKI, G., AND THOME, J. R. Two-Phase Flow Patterns and Flow-Pattern Maps: Fundamentals and Applications. *Applied Mechanics Reviews 61*, 5 (07 2008). 050802.
[14] CLOTTES, J., BELTRÁN, A., COURTIN, J., AND COSQUER, H. La grotte cosquer (cap morgiou, marseille). *Bulletin de la Société préhistorique française 89*, 4 (1992), 98–128.
[15] COQUEL, F., GALLOUËT, T., HÉRARD, J.-M., AND SEGUIN, N. Closure laws for a two-fluid two-pressure model. *Comptes Rendus Mathematique 334*, 10 (2002), 927–932.
[16] CORDIER, F., DEGOND, P., AND KUMBARO, A. An asymptotic-preserving all-speed scheme for the euler and navier–stokes equations. *Journal of Computational Physics 231*, 17 (2012), 5685–5704.
[17] CRUM, L. A. The polytropic exponent of gas contained within air bubbles pulsating in a liquid. *The Journal of the Acoustical Society of America 73*, 1 (1983), 116–120.
[18] DE O. FALCÃO, A. F. Wave energy utilization: A review of the technologies. *Renewable and Sustainable Energy Reviews 14*, 3 (2010), 899–918.
[19] DEMAY, C., AND HÉRARD, J.-M. A compressible two-layer model for transient gas–liquid flows in pipes. *Continuum Mechanics and Thermodynamics 29*, 2 (Mar 2017), 385–410.
[20] GODLEWSKI, E., PARISOT, M., SAINTE-MARIE, J., AND WAHL, F. Congested shallow water model: roof modeling in free surface flow. *ESAIM: Mathematical Modelling and Numerical Analysis 52*, 5 (Sep 2018), 1679–1707.
[21] GODLEWSKI, E., PARISOT, M., SAINTE-MARIE, J., AND WAHL, F. Congested shallow water model: on floating body. *The SMAI journal of computational mathematics 6* (2020), 227–251.
[22] GOPAL, C., MOHANRAJ, M., CHANDRAMOHAN, P., AND CHANDRASEKAR, P. Renewable energy source water pumping systems—a literature review. *Renewable and Sustainable Energy Reviews 25* (2013), 351–370.
[23] HAACK, J., JIN, S., AND LIU, J. An all-speed asymptotic-preserving method for the isentropic euler and navier-stokes equations. *Communications in Computational Physics 12*, 4 (2012), 955–980.
[24] HERBIN, R., KHERIJI, W., AND LATCHÉ, J.-C. On some implicit and semi-implicit staggered schemes for the shallow water and euler equations. *ESAIM: M2AN 48*, 6 (2014), 1807–1857.
[25] KARNI, S., KIRR, E., KURGANOV, A., AND PETROVA, G. Compressible two-phase flows by central and upwind schemes. *ESAIM: Mathematical Modelling and Numerical Analysis 38*, 3 (2004), 477–493.
[26] LANNES, D. On the dynamics of floating structures. *Annals of PDE 3*, 1 (2017), 11.
[27] LANNES, D., AND BONNETON, P. Derivation of asymptotic two-dimensional time-dependent equations for surface water wave propagation. *Physics of Fluids 21*, 1 (2009).
[28] LUGLI, F., AND ZERBETTO, F. An introduction to bubble dynamics. *Phys. Chem. Chem. Phys. 9* (2007), 2447–2456.
[29] MURAKAMI, M., AND MINEMURA, K. Effects of entrained air on the performance of a horizontal axial-flow

pump. *Journal of Fluids Engineering 105*, 4 (1983), 382.

[30] PARISOT, M. Entropy-satisfying scheme for a hierarchy of dispersive reduced models of free surface flow. *International Journal for Numerical Methods in Fluids 91*, 10 (2019), 509–531.

[31] PARISOT, M., AND VILA, J.-P. Centered-potential regularization for the advection upstream splitting method. *SIAM Journal on Numerical Analysis 54*, 5 (2016), 3083–3104.

[32] PEYRÉ, G., AND CUTURI, M. Computational optimal transport. *Foundations and Trends in Machine Learning, vol. 11, no. 5-6, pp. 355-607, 2019* (03 2018).

[33] PROSPERETTI, A., CRUM, L. A., AND COMMANDER, K. W. Nonlinear bubble dynamics. *The Journal of the Acoustical Society of America 83*, 2 (1988), 502–514.

[34] ROLLER, S., AND MUNZ, C.-D. A low mach number scheme based on multi-scale asymptotics. *Computing and Visualization in Science 3*, 1 (2000), 85–91.

[35] SAMBA, B., MATHURIN, D., AND MUSANDJI, F. Numerical modeling of mixed flows in storm water systems: Critical review of literature. *Journal of Hydraulic Engineering 139*, 4 (2022/08/06 2013), 385–396.

[36] THOMANN, A., PUPPO, G., AND KLINGENBERG, C. An all speed second order well-balanced imex relaxation scheme for the euler equations with gravity. *Journal of Computational Physics 420* (2020), 109723.

[37] WENNEKER, I., SEGAL, A., AND WESSELING, P. A mach-uniform unstructured staggered grid method. *International Journal for Numerical Methods in Fluids 40*, 9 (2002), 1209–1235.